PIER C

(Received 31 May 2026, Accepted 17 June 2026, Scheduled 1 July 2026)

Ceramic Filter Based on Coupled Slots and Two Sets of Triple Blind Holes

Yunxiu Wang*, Wei Chao Yang, Yang Gao, Jianni Zhang, and Ling Tang

School of Electronic and Information Engineering, China West Normal University, Nanchong 637009, China

ABSTRACT: A novel ceramic waveguide filter using coupled slots and two sets of cascade quadruple (CQ) coupling units is presented in this study. Owing to this CQ structure, there are two pairs of transmission zeros at the edge of the passband to ensure that the filter has good selectivity. First, the effect of cavity dimensions on the resonant frequencies of the intrinsic modes was analyzed. Next, the impact of the coupling structure on the coupling bandwidth and the characteristics of the electric-field distribution was explored, followed by an examination of the relationship between the feeding structure and the quality factor (Qe). Finally, a prototype filter centered at 3.5 GHz with a bandwidth of 200 MHz was designed and fabricated. The insertion loss within the passband was less than 1.9 dB, and the return loss was greater than 20 dB. The out-of-band suppression exceeds 42 dB in 3.3–3.36 GHz and 3.64–3.7 GHz, and even exceeds 70 dB in 3.2–3.3 GHz and 3.7–3.8 GHz.

1. INTRODUCTION

Radio frequency (RF) filters are indispensable in wireless communication, radar, electronic countermeasures, and aerospace applications [1–5]. Miniaturization, low in-band insertion loss, highly attenuated stopbands, and sharpened rejection skirts in close proximity to the passband are several fundamental requirements in filter design [6–9]. Recently, ceramic dielectric filters have attracted widespread attention owing to their compact structure, high Q-factor, and stable performance [10–12]. In addition to being used in traditional mobile communication base stations and consumer electronic devices, ceramic filters are highly attractive in systems, such as smart phones, smart watches, spacecraft, and satellite communications, which require extremely light weight, high integration, and extreme temperature stability. It can be processed into various complex structures using 3D printing technology to provide some customized performance.

The concept of dielectric resonators was first introduced by Richmyer in 1939, who demonstrated that a dielectric rod could serve as part of a resonator [13]. Since then, advances in ceramic materials have led to the development of various ceramic filters that exhibit superior performance and broad applicability in practical applications [14–20]. In [14], Wang et al. designed a high-Q dielectric filter based on cylindrical ceramic dielectric waveguide resonators. This filter employs a monolithic surface-metallized ceramic dielectric mounted on a printed circuit board (PCB) using reflow soldering technology, ensuring stable performance and a high Q-factor. Ref. [15] introduced a novel narrowband balanced bandpass filter (BPF) based on two coupled rectangular dielectric resonators (DR). By exploiting the differential excitation of the fundamental mode of the DR, this filter achieves excellent out-of-band suppression. Additionally, Xu et al. proposed a compact dual-band passband filter (BPF) in [16] utilizing a dual-mode dielectric waveguide resonator (DWR). By adjusting the radius and height of the cylindrical DWR, the operating frequency can be independently controlled, thereby offering flexible frequency tuning.

The design method for generating transmission zeros using cross-coupling technology has emerged as a prominent area of research, drawing significant attention [17–24]. In [21], Yuan introduced a cascade quadruple (CQ) structure, which employs a single blind hole between two resonant cavities to achieve electrical coupling. The coupling strength can be easily adjusted by modifying the depth of the blind hole. However, this structure is not suitable for scenarios requiring low coupling. To overcome this limitation, Liang et al. in [22] proposed a six-cavity ceramic filter that combines blind holes and coupling slots. This design achieved a fractional bandwidth (FBW) of 5.71% and a band-stop attenuation of $\geq$ 51 dB in the 3.2–3.3 GHz and 3.7–3.8 GHz ranges. Due to its wider coupling bandwidth than 100 MHz, this method has been widely adopted in base station applications [22–26]. In [23], a conical electrical coupling blind hole was introduced to design an eight-cavity ceramic filter with two transmission zeros, ensuring excellent isolation. The electrical coupling bandwidth can be adjusted by altering the metal coating area of the conical hole and the depth of the cylindrical hole. However, this filter is difficult to manufacture and challenging to tune. Ref. [24] proposed a capacitive coupling method by placing an isolated metal strip within a window etched on the silver surface. While this method improves out-of-band suppression, it still suffers from electromagnetic leakage. Finally, [25] introduced a ceramic rectangular block, where a blind hole is coated with a silver layer, and a non-metalized ring gap is etched around the blind hole, making the surface metal of the blind hole physically isolated. Four varactors bridge the gap and connect the blind hole and the other part of the resonator. Based on the above structure, they designed a six-pole tunable cascade quadruplet filter and a cascade triplet filter.

* Corresponding author: Yunxiu Wang (627662147@qq.com).

In this study, an eight-cavity ceramic filter was designed, employing two types of three-blind-hole structures symmetrically positioned on opposite sides of a rectangular ceramic block to provide electric coupling. First, the relationship between the resonant frequency and its structural size was obtained by analyzing the intrinsic modes of a single cavity. Second, the coupling structures between the cavities were discussed. The feeding structure was then designed. Finally, a prototype filter was designed and fabricated. The measured results show that the filter has excellent selectivity. The ceramic used here has a relative permittivity of 20.3 and a loss tangent of 6×10^{-4}.

2. ANALYSIS AND DESIGN

The systematic synthesis design procedure follows four steps, as discussed and documented in [23]. The characteristics of the designed filter are summarized in Table 1. The filter operates at 3.5 GHz; the 3 dB bandwidth and relative bandwidth are 200 MHz and 5.7% respectively; the insertion loss within the passband is less than 2 dB; the return loss is greater than 17 dB; the group delay is less than 25 ns in the ranges of 3.4 GHz to 3.6 GHz. The out-of-band suppression in the range of 3.3 $\sim$ 3.36 GHz and 3.64 $\sim$ 3.7 GHz is greater than 38 dB and greater than 62 dB in 3.2 $\sim$ 3.3 GHz and 3.7 $\sim$ 3.8 GHz. To achieve the above technical specifications, eight resonators were used, and their topological structure is shown in Figure 1. S and L represent the feeding ports.

TABLE 1. The technical specifications.

Design Parameters	Values
f_0 (GHz)	3.5
BW (MHz)	200
FBW (%)	5.7
IL (dB)	≤ 2
RL (dB)	≥ 17
Group Delay τ (ns)	≤ 25 (3.4 GHz–3.6 GHz)
suppression (dB)	≥ 38 (3.3–3.36 GHz and 3.64–3.7 GHz)
suppression (dB)	≥ 62 (3.2–3.3 GHz and 3.7–3.8 GHz)

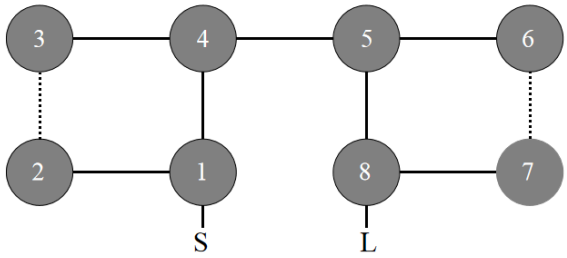

FIGURE 1. Topology of the filter.

The relationship between external quality factors and coupling matrix is

$$Q_{S,1} = \frac{1}{M_{S,1}^2 \cdot FBW} = Q_{8,L} = \frac{1}{M_{8,L}^2 \cdot FBW} \tag{1}$$

$M_{S,1}$ is the coupling coefficient between source and resonator 1, and $M_{8,L}$ represents the coupling coefficient between the eighth resonator and load. The fractional bandwidth FBW is defined as

$$FBW = (f_H - f_L)/f_0 \tag{2}$$

where f_H and f_L are the upper and lower cutoff frequencies, respectively, and f_0 is the central frequency.

Because the coupling bandwidth CBW can also represent the coupling between cavities, we can choose it as the design parameter. It satisfies the following relationship

$$CBW = f_2 - f_1 \tag{3}$$

f_2 and f_1 represent the eigenfrequencies obtained from the eigenmode solver.

By inputting the technical parameters from Table 1 into SynMatrix Desktop, the coupling matrix M, coupling bandwidths $CBW_{m,n}$, and external quality factors Q can be obtained, as shown in (4) and Table 2, respectively. $Q_{S,1}$ and $Q_{8,L}$ denote the external quality factors of the input and output resonators, respectively. $CBW_{m,n}$ is the coupling bandwidth between the m-th and n-th resonators. During the simulation, the start frequency was set to 3395.0 MHz, and the stop frequency was 3605.0 MHz.

$$M = \begin{array}{c} \\ S \\ 1 \\ 2 \\ 3 \\ 4 \\ 5 \\ 6 \\ 7 \\ 8 \\ L \end{array} \begin{array}{c} \begin{array}{cccccccccc} S & 1 & 2 & 3 & 4 & 5 & 6 & 7 & 8 & L \end{array} \\ \begin{bmatrix} 0 & 1.06 & 0 & 0 & 0 & 0 & 0 & 0 & 0 & 0 \\ 1.06 & 0 & 0.86 & 0 & 0.22 & 0 & 0 & 0 & 0 & 0 \\ 0 & 0.86 & 0 & -0.74 & 0 & 0 & 0 & 0 & 0 & 0 \\ 0 & 0 & -0.74 & 0 & 0.51 & 0 & 0 & 0 & 0 & 0 \\ 0 & 0.22 & 0 & 0.51 & 0 & 0.54 & 0 & 0 & 0 & 0 \\ 0 & 0 & 0 & 0 & 0.54 & 0 & 0.54 & 0 & 0.08 & 0 \\ 0 & 0 & 0 & 0 & 0 & 0.54 & 0 & -0.66 & 0 & 0 \\ 0 & 0 & 0 & 0 & 0 & 0 & -0.66 & 0 & 0.88 & 0 \\ 0 & 0 & 0 & 0 & 0 & 0.08 & 0 & 0.88 & 0 & 1.06 \\ 0 & 0 & 0 & 0 & 0 & 0 & 0 & 0 & 1.06 & 0 \end{bmatrix} \end{array} \tag{4}$$

The filter consists of two distinct CQ structures, which enable it to generate two pairs of tunable transmission zeros, effectively meeting the stringent design requirements of modern 5G base stations while offering customizable out-of-band rejection characteristics.

TABLE 2. Relevant theoretical model parameters (in MHz).

Parameter	Value	Parameter	Value
$Q_{S,1}$	14.73	$CBW_{4,5}$	114
$Q_{8,L}$	14.73	$CBW_{5,6}$	114
$CBW_{1,2}$	180	$CBW_{5,8}$	17
$CBW_{1,4}$	45	$CBW_{6,7}$	−139
$CBW_{2,3}$	−155	$CBW_{7,8}$	185
$CBW_{3,4}$	107		

2.1. The Single-Cavity Structure Design and Analysis

Because the characteristics of ceramic dielectric waveguide filters are similar to those of rectangular metallic filters, the resonant frequency of the resonator is given by [28]

$$f_{mnp} = \frac{1}{2\sqrt{\mu_r \varepsilon_r}} \sqrt{\left(\frac{m\pi}{a}\right)^2 + \left(\frac{n\pi}{b}\right)^2 + \left(\frac{p\pi}{l}\right)^2} \quad (5)$$

where μ_r and ε_r denote the relative magnetic permeability and dielectric constant of the ceramic material, respectively; a, b, and l are the dimensions along the X, Y, and Z axes, respectively; m, n, and p indicate the numbers of half-wavelengths in the X, Y, and Z directions, respectively.

It is Mode 1 when $m = 1$, $n = 0$, and $p = 1$, named as the main mode TE_{101}, while Modes 2 and 3 correspond to the higher-order modes. If set $l = a$, $b = a/2$, $\varepsilon_r = 20.3$, and $\mu_r = 1$, a can be calculated as 13.4 mm when the center frequency is 3.5 GHz according to (5).

A cylindrical hole with a diameter of 4 mm and depth of H_T was now drilled at the center of the dielectric block, as shown in Figure 2.

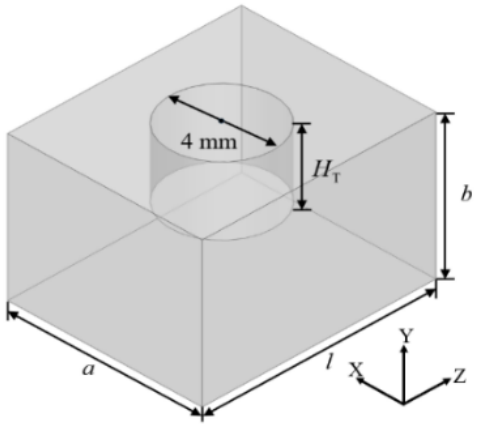

FIGURE 2. Single cavity.

Eigenmode analysis of the resonant cavity was performed using Softwave High Frequency Structure Simulator (HFSS) to investigate how the parameters a, b, l, and H_T affect the resonant frequency of each mode, as depicted in Figure 3.

It can be observed from Figure 3 that the resonant frequencies of all the three modes vary with the changes in a, b, l, and H_T, but the resonant frequencies of modes 2 and 3 are much higher than 3.5 GHz and have almost no effect on the main mode TE_{101}. If there is a coupling between resonators, the resonant frequencies of modes 2 and 3 will be different from those without coupling.

2.2. The Coupling Structure Design and Analysis

As shown in Figure 4(a), three holes are drilled along the central axis AA' of resonators 2 and 3, with the larger hole in the middle having a radius of r_{s1} and a depth of h_{s1}. The two symmetrical smaller holes have a diameter of r_{m1} and a depth of h_{m1}, and the distance between the large and small holes is a_{x1}. Figure 4(b) shows the cross-section. To observe the field distribution inside the cavity more clearly, the block was divided into two parts along BB'. The field distribution of the main mode is shown in Figure 4(c). It can be observed that the main mode is an odd mode, and the coupling between resonators 2 and 3 is electrical coupling. Similarly, there are three holes between resonators 6 and 7, as shown in the cross-section in Figure 5. Unlike before, the larger hole in the middle is punched from below, whereas the small holes on both sides are punched from above. As shown in Figure 5(c), the main mode is an odd mode, and electrical coupling is achieved between resonators 6 and 7.

Considering that the coupling between the two resonators is symmetrical, the coupling coefficient $M_{i,j}$ is defined as

$$M_{i,j} = \frac{f_2^2 - f_1^2}{f_2^2 + f_1^2} \quad (6)$$

In the case where an odd mode is excited, the two cavities have opposite voltages, making the symmetry plane an electric wall, as indicated in Figure 4(c) and Figure 5(c).

Figure 6 displays the impact of the physical dimensions on the coupling bandwidths. The research schemes are shown in Table 3. As shown in Figure 6(a), the electric coupling bandwidths *CBW*s increase as h_s increases. The variations caused by h_{s1} were greater than a_x. Additionally, Figure 6(b) indicates that h_{m2} has a greater effect on the *CBW*s than h_{m1}. Figure 6(c) reveals that the electric coupling strengths gradually decrease as a_x increases. The results, as shown in Figure 6(d), indicate that the *CBW*s generally grow when r_{s1} rises, while the *CBW*s generally decrease as r_{s2} increases. As shown in Figure 6(e), the increase in r_m causes the electric coupling strength to increase. The experiment demonstrated that fine-tuning the electrical *CBW*s can be achieved by adjusting h_s, h_m, a_x, r_s, and r_m of the two sets of three-blind-hole structure.

As discussed above, electrical coupling is achieved through coupling holes, whereas coupled slots are widely used to realize magnetic coupling [22–27]. The structural diagram of the coupled slot and the electric field distribution of the main mode are shown in Figure 7(a) and Figure 7(b), respectively. As shown in Figure 7(c) and Figure 7(d), the magnetic coupling bandwidth gradually decreases as L and W increase.

Another way to configure the coupled slot is to place it in the center, with L remaining constant and moving Δy_d to allow fine adjustment, as shown in Figure 8(a). Figure 8(b) shows that the greater the absolute value Δy_d along the central line, the wider the magnetic coupling bandwidth.

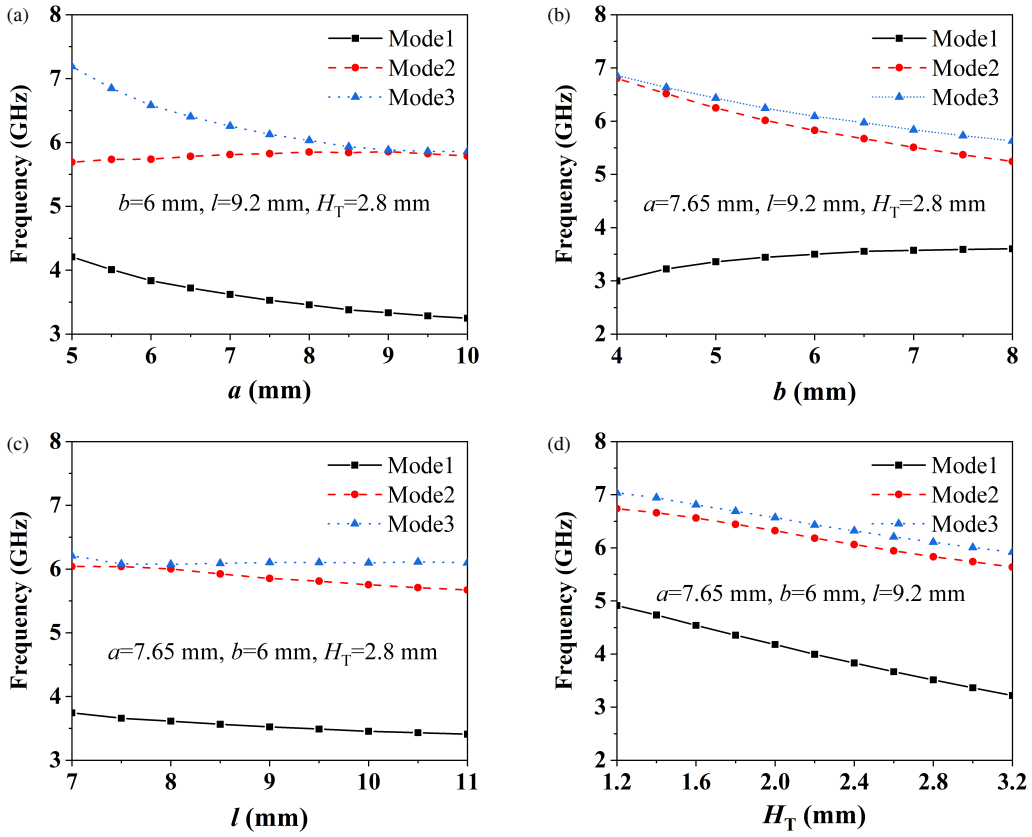

FIGURE 3. Resonant frequencies in the single-cavity. (a) Different lengths, a, (b) different lengths, b, (c) different lengths, l, and (d) different lengths, H_T.

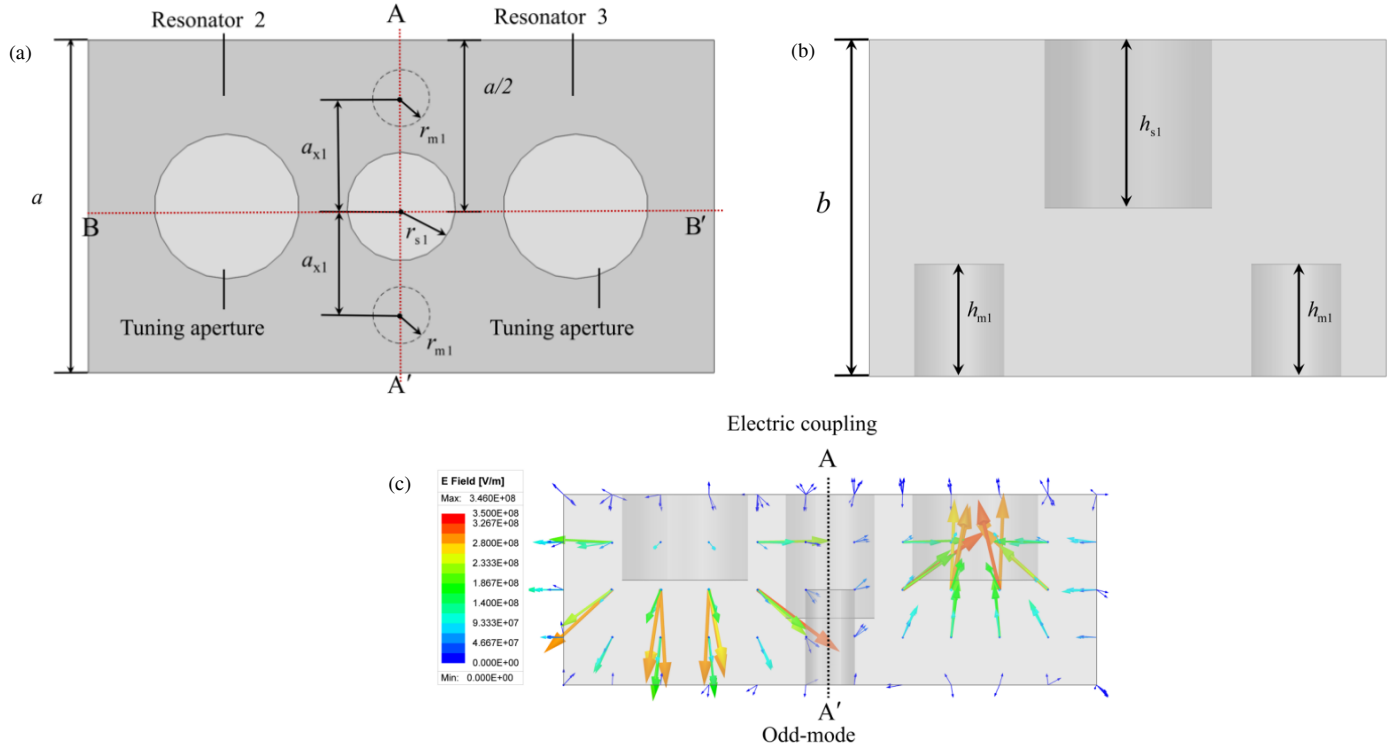

FIGURE 4. Resonators 2 and 3 (a) Top view, (b) cross-section, and (c) field distribution of the main mode.

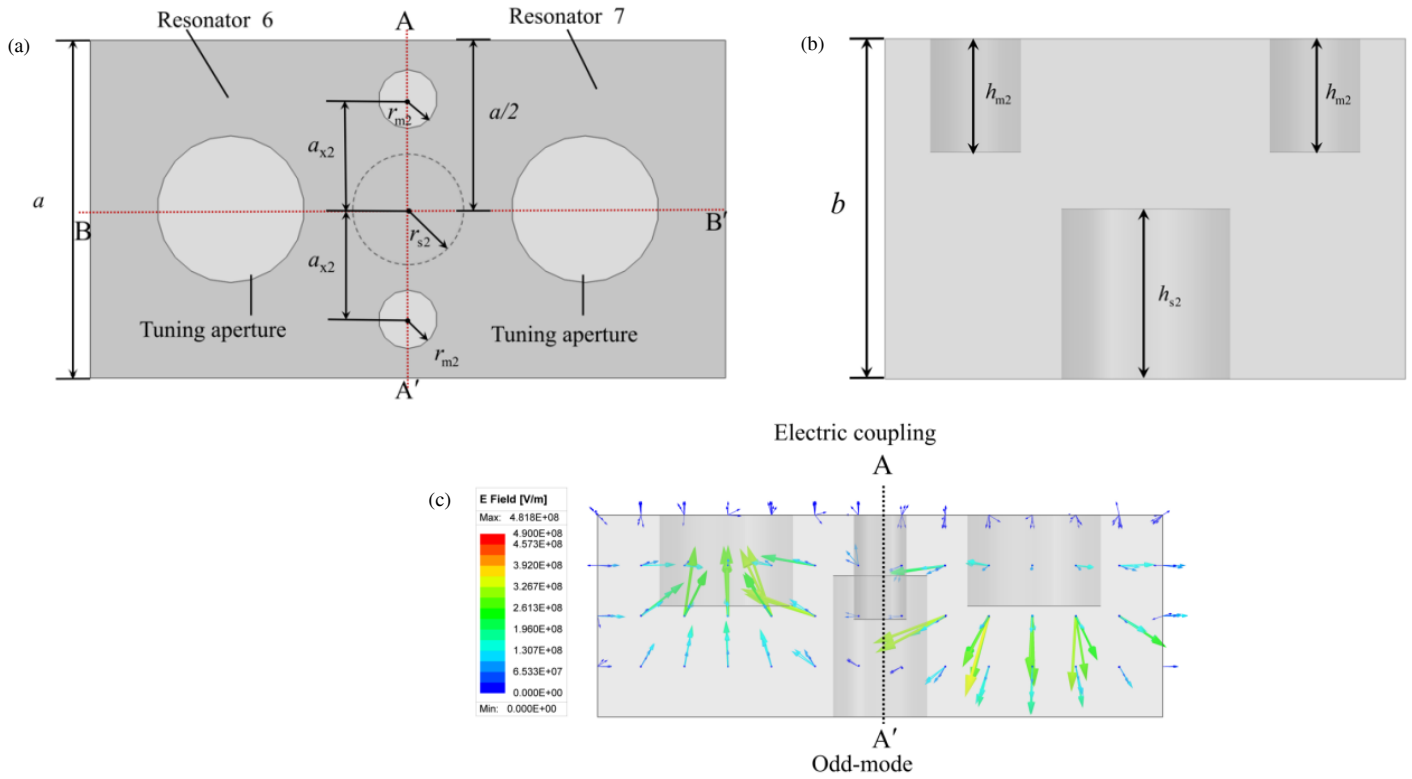

FIGURE 5. Resonators 6 and 7. (a) Top view, (b) cross-section, and (c) field distribution of the main mode.

TABLE 3. The research scheme of the coupling structure size (in mm).

Resonators 2 and 3				Resonators 6 and 7					
h_{s1}	h_{m1}	a_{x1}	r_{s1}	r_{m1}	h_{s2}	h_{m2}	a_{x2}	r_{s2}	r_{m2}
$1.0 \sim 6.0$	3.0	3.0	1.4	0.8	$1.0 \sim 6.0$	3.1	3	1.4	0.8
3.9	$1.0 \sim 3.0$	3.0	1.4	0.8	4.2	$1.0 \sim 3.0$	3	1.4	0.8
3.9	3.0	$2.6 \sim 3.6$	1.4	0.8	4.2	3.1	$2.6 \sim 3.6$	1.4	0.8
3.9	3	3	$0.6 \sim 1.6$	0.8	4.2	3.1	3	$0.6 \sim 1.6$	0.8
3.9	3.0	3.0	1.4	$0.5 \sim 1.1$	4.2	3.1	3.0	1.4	$0.5 \sim 1.1$

2.3. The Feeding Structure Design and Analysis

A probe was inserted into resonators 1 or 8, as shown in Figure 9. Figure 10 shows that the insertion depth and position of the probe influence the external quality factor Q_e. The relationship between the group delay and external quality factor is given by [29]

$$Q_e = \frac{\omega_0 \tau_{\max}}{4} = \frac{\pi f_0 \tau_{\max}}{2} \tag{7}$$

where $\tau_{\max}$ is the maximum group delay at resonance. Therefore, based on the group delay required by Table 1 and the external quality calculated by Table 2, the position of the feed probe can be determined.

2.4. Design of Eight-Cavity Ceramic Waveguide Filter

Based on the above analysis, we first constructed an eight-cavity filter model. The eigenmode solver determined the cavity dimensions as $a = 9.2\,\text{mm}$, $b = 6\,\text{mm}$, $l = 7.65\,\text{mm}$, and $H_T = 2.77\,\text{mm}$. Subsequently, different electric and magnetic coupling structures are selected according to the required CBWs, with the appropriate initial dimensions and blind-hole depths calculated via simulation. Using the obtained $Q_e = 14.73$, we calculated a probe feed depth of $F_d = 2.1\,\text{mm}$, with offset values in both the x and y directions set to be $F_x = F_z = 0.2\,\text{mm}$. Finally, an optimized model of the eight-cavity ceramic waveguide filter was developed, as shown in Figure 11. Table 4 lists the detailed parameters, with H_{Tn} indicating the depth of the n-th tuning blind hole.

As illustrated in Figure 11(a), the width of all coupled slots was $W = 1.5\,\text{mm}$. The overall dimensions of the designed filter were $41.3 \times 18.3 \times 6\,\text{mm}^3$. This configuration forms two CQ structures, thereby generating two pairs of adjustable transmission zeros, which guarantees that the constituted filter has sharp roll-off skirts outside the desired passband.

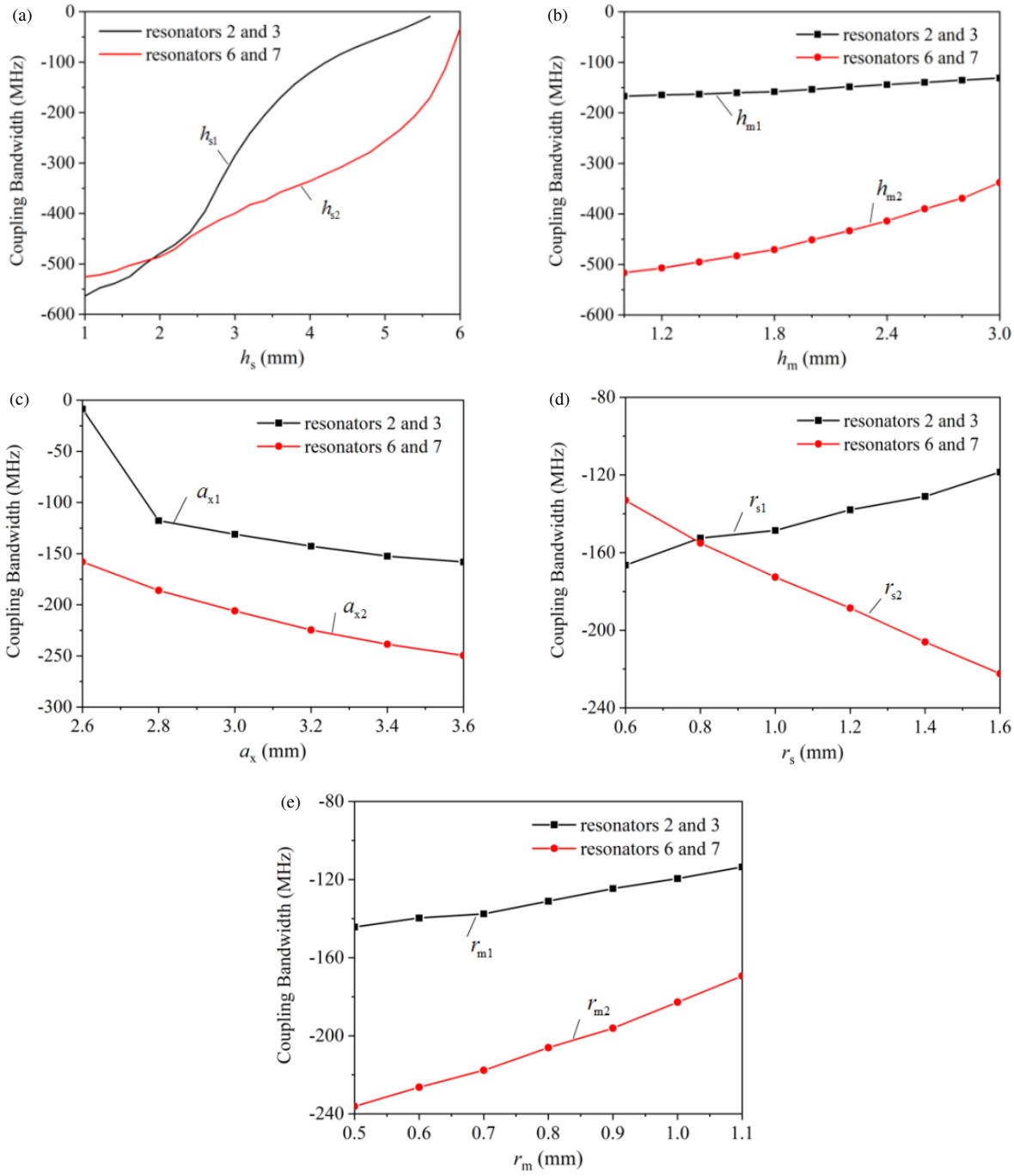

FIGURE 6. The simulated coupling bandwidths with different sizes in Table 3. (a) With different h_{s1} and h_{s2}, (b) with different h_m, (c) with different a_x, (d) with different r_s, and (e) with different r_m.

3. MEASUREMENT RESULTS AND DISCUSSION

Figure 12 shows a photograph of the fabricated filter. Figure 13 shows the simulated and measured results. It can be seen that its center frequency is 3.5 GHz, with a bandwidth of 200 MHz and a return loss $\geq$ 20 dB. Within 3.4 $\sim$ 3.6 GHz, the insertion loss is maintained $\leq$ 1.9 dB. Furthermore, in 3.2–3.3 and 3.7–3.8 GHz, the filter exhibits excellent suppression, achieving $\geq$ 70 dB. Additionally, within 3.3–3.36 GHz and 3.64–3.7 GHz, the suppression level is $\geq$ 42 dB. As shown in Figure 13(b), the group delay of the filter is $\leq$ 25 ns within 3.4–3.6 GHz. It can be observed that the simulated and measured results show a slight frequency shift. This slight shift may be due to fabrication accuracies and added input/output subminiature A (SMA) connectors.

To demonstrate the performance of the filter, we compared it with the other filters listed in Table 5. It shows that the filter has a compact size and excellent out-of-band rejection. These outstanding features make it an ideal choice for meeting the

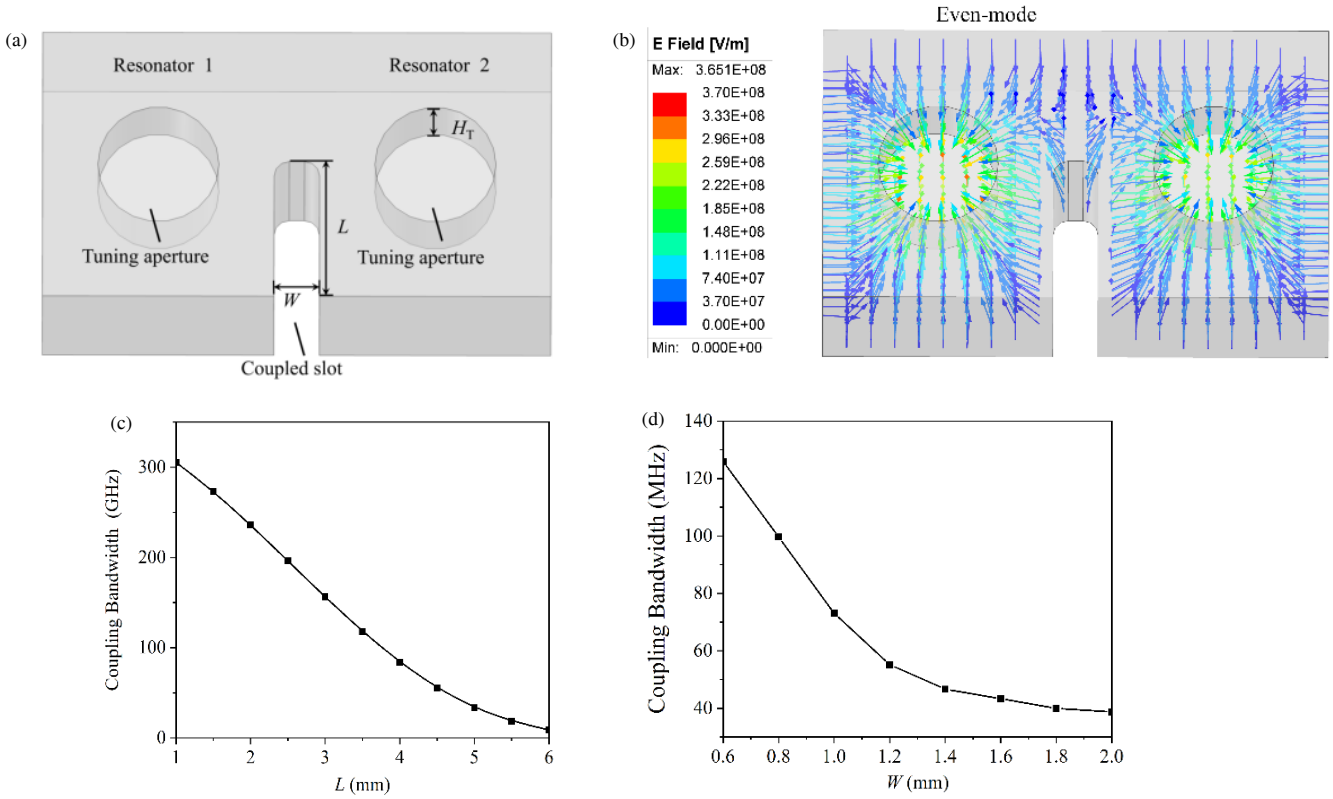

FIGURE 7. (a) Coupled slot, (b) field distribution of main mode, (c) coupling bandwidth with different L, and (d) coupling bandwidth with different W.

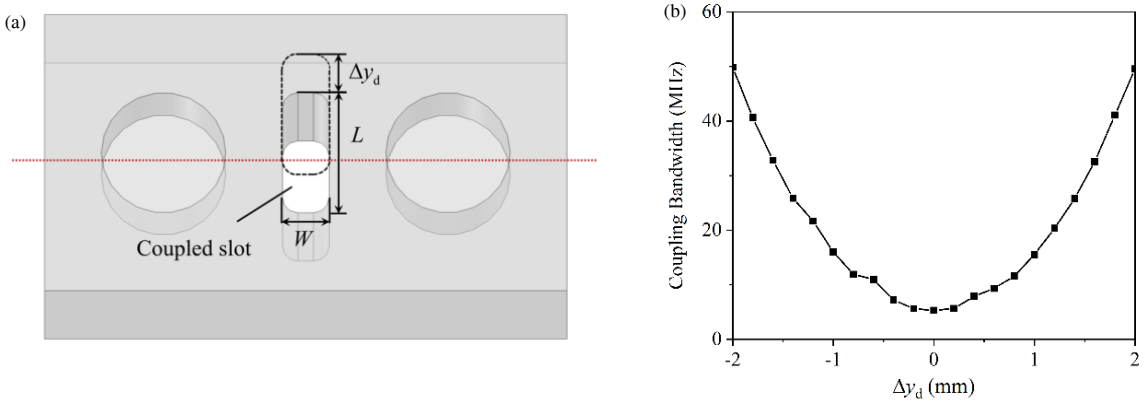

FIGURE 8. (a) Coupled slot and (b) the relationship between Δy_d and the coupling bandwidth.

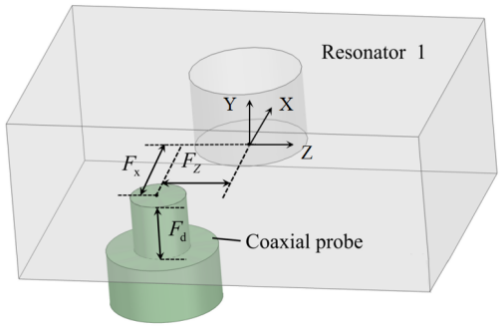

FIGURE 9. Schematic diagram of the feeding probe structure.

high-performance and miniaturization requirements of current 5G base station communication equipment. Table 6 shows the comparison with ceramic waveguide filter and low-temperature co-fired ceramic filter (LTCC). The main advantages of ceramic waveguide filters used for 5G base stations are small size, light weight, high Q value, low loss, and good temperature stability. They are sensitive to manufacturing tolerance and require careful debugging in the later stage. LTCC, which is mainly used for mobile terminals, Internet of Things (IoT), and Wi-Fi devices, has extremely high integration and low cost, but its power is low, and the loss at high frequencies will increase.

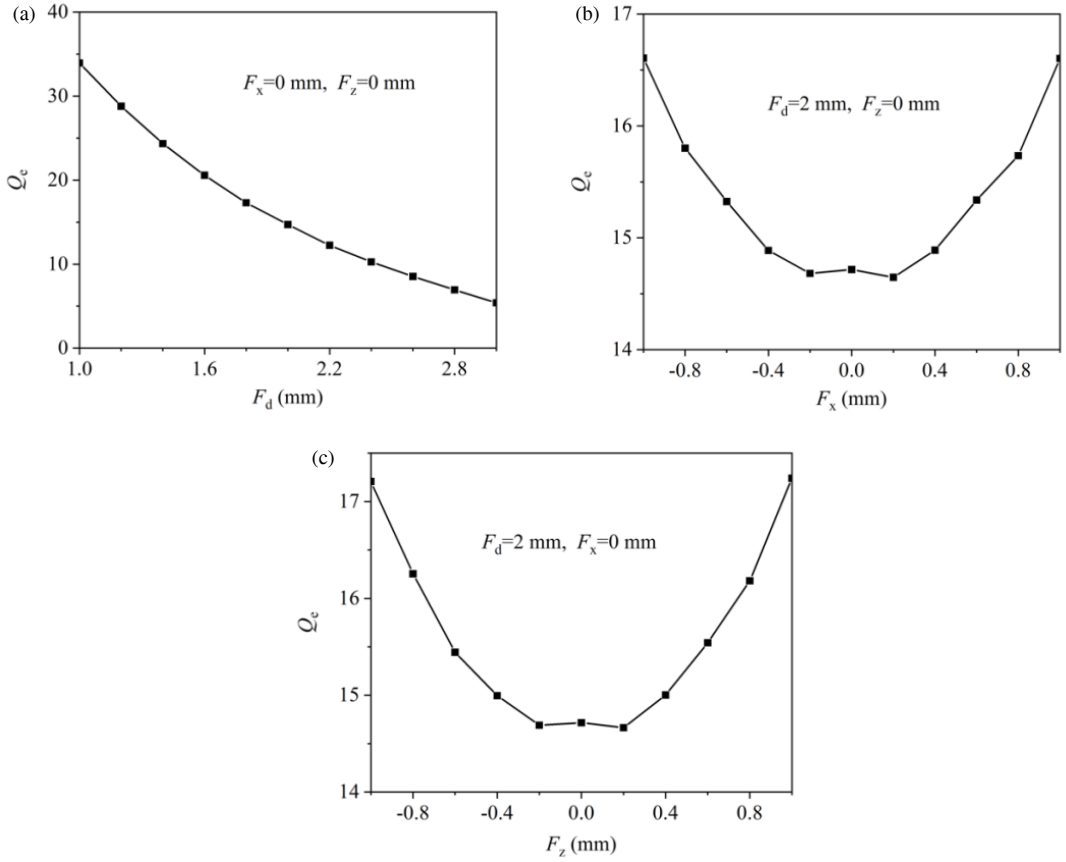

FIGURE 10. (a)–(c) Simulated Q_e with different F_d, F_x, and F_z.

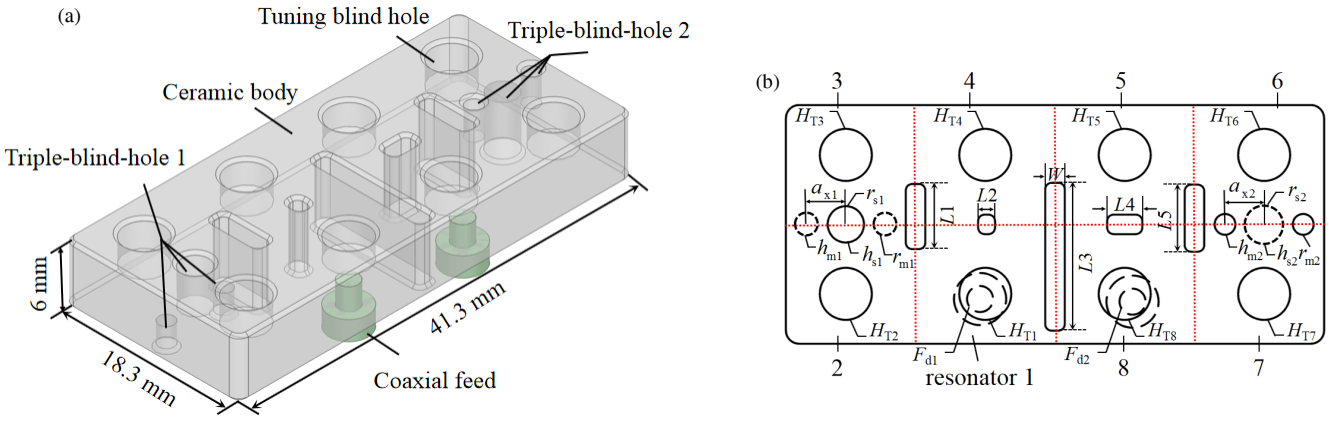

FIGURE 11. (a) Simulation model and (b) diagram of the optimized filter structure.

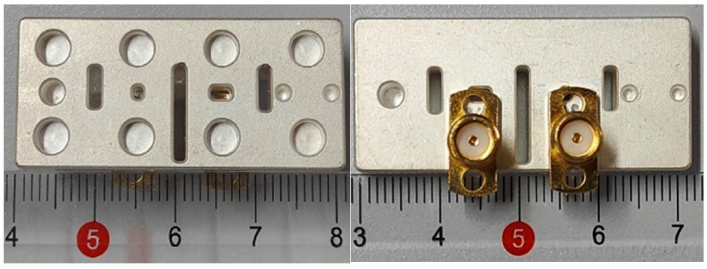

FIGURE 12. The manufactured filter.

TABLE 4. Structural parameters of the filter (in mm).

Symbol	Value	Symbol	Value	Symbol	Value
H_{T1}	2.33	$L1$	6.00	h_{s1}	3.90
H_{T2}	2.70	$L2$	1.30	h_{m1}	2.30
H_{T3}	2.77	$L3$	11.34	a_{x1}	3.00
H_{T4}	2.39	$L4$	2.70	r_{s1}	1.40
H_{T5}	2.45	$L5$	5.15	h_{s2}	5.40
H_{T6}	2.74	F_{d1}	2.25	h_{m2}	3.10
H_{T7}	2.69	F_{d2}	2.10	a_{x2}	3.00
H_{T8}	2.43	r_{m1}	0.80	r_{s2}	1.40
W	1.50	r_{m2}	0.80		

TABLE 5. The comparison between the filter and other 5G base station filters.

Ref	[23]	[24]	[25]	[26]	[27]	Proposed
Order	8	10	6	4	8	8
f_0 (GHz)	3.5	2.595	3.4–3.82	3.5	3.5	3.5
FBW (%)	5.71	6.20	3.50	5.70	5.41	5.71
IL (dB)	≤ 2.0	≤ 2.2	$\leq 6.5-11$	≤ 0.5	≤ 0.1	≤ 1.9
RL (dB)	≤ 19	≤ 20	≤ 17	≤ 20	≤ 17.3	≤ 20
Transmission zeros	-	-	2	2	2	4
Near-end out-of-band suppression (dB)	≥ 39	≥ 40	≥ 28	≥ 22	≥ 60	≥ 42
Far-end out-of-band suppression (dB)	≥ 63	≥ 65	≥ 55	≥ 45	≥ 70	≥ 70
Volume (cm^3)	4.788	6.009	3.756	3.645	5.292	4.535

TABLE 6. The comparison with LTCC.

Characteristic	Ceramic waveguide filter	LTCC
Technology	High	High
Application	5G base station	Mobile terminals, IoT devices, WI FI
Manufacturing complexity	Moderate to high	Moderate
Key advantage	Small size, light weight, high Q value, low loss, good temperature stability	Integration, low cost
Main challenges	Sensitive to manufacturing tolerance	Low power tolerance, high interlayer alignment requirements, and possible increase in losses at high frequencies
Relative cost	Moderate	Lower

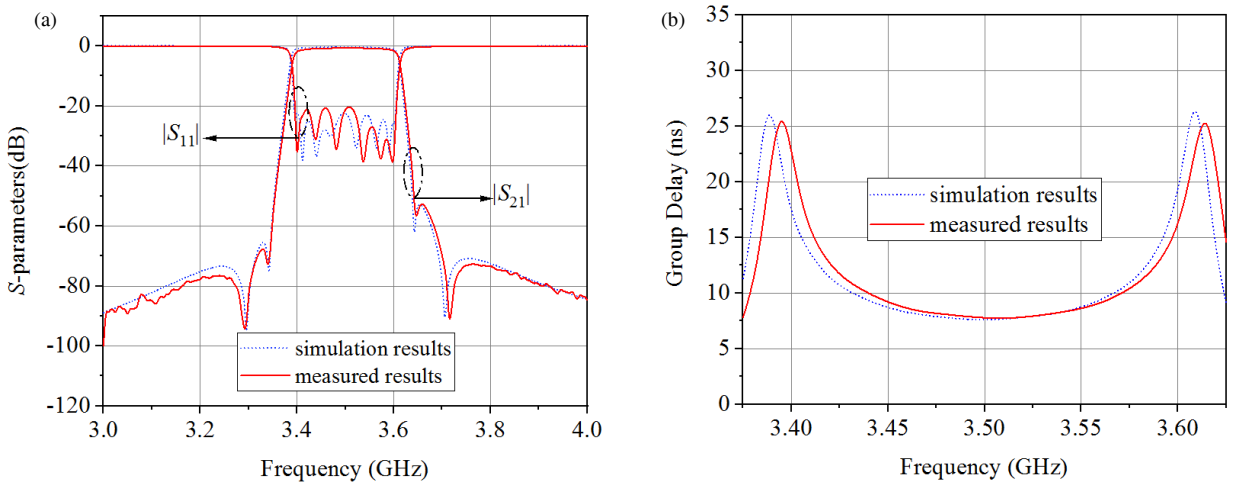

FIGURE 13. The experimental and simulation results. (a) S-parameters and (b) group delay.

4. CONCLUSION

In this study, we propose an eight-cavity ceramic waveguide filter, consisting of two CQ cavity structures, which generates two pairs of transmission zeros, ensuring excellent out-of-band suppression characteristics. Electrical coupling is achieved using two types of three-blind-hole coupling structures. The coupling bandwidth can be adjusted by modifying the radius, depth, and spacing of blind holes. The adjustment precision reaches 1.5 MHz, thereby meeting the design requirements for high-performance ceramic waveguide filters. The measured frequency responses of the fabricated filter justified the design method and simulated results. The designed filter has a compact size and has excellent in-band and out-of-band performance, making it suitable for 5G base stations.

ACKNOWLEDGEMENT

This work was supported by the Fundamental Research Funds of China West Normal University (24kx007) and Sichuan Provincial Natural Science Foundation (26NSFSC0072).

REFERENCES

[1] He, W., J. Zhao, X. Chen, H. Yang, L. Sang, Z. Li, S. Wang, and W. Huang, "Soft radio frequency microstrip bandpass filter: Precise design and demonstration," *AIP Advances*, Vol. 13, No. 12, 125214, 2023.

[2] Hussein, O. I., K. A. A. Shamaileh, N. I. Dib, A. Nosrati, S. Abushamleh, D. G. Georgiev, and V. K. Devabhaktuni, "Substrate integrated waveguide bandpass filtering with Fourier-varying via-hole walling," *IEEE Access*, Vol. 8, 139 706–139 714, 2020.

[3] Yadav, S., M. Sharma, and B. K. Kuanr, "Reconfigurable bandpass filter using Ce-doped YIG ferrites for wideband applications," *Journal of Applied Physics*, Vol. 134, No. 4, 043902, 2023.

[4] Chen, R.-S., S.-W. Wong, J.-Y. Lin, Y. Yang, Y. Li, L. Zhang, Y. He, and L. Zhu, "Reconfigurable cavity bandpass filters using fluid dielectric," *IEEE Transactions on Industrial Electronics*, Vol. 68, No. 9, 8603–8614, 2021.

[5] Shen, G., W. Che, W. Feng, Y. Shi, Y. Shen, and F. Xu, "A miniaturized Ka-band bandpass filter using folded hybrid resonators based on monolithic microwave integrated circuit technology," *IEEE Transactions on Circuits and Systems II: Express Briefs*, Vol. 68, No. 6, 1778–1782, 2021.

[6] Cheng, S. M. and D. Psychogiou, "Compact multi-band filter/diplexer LNAs using split-type multi-resonant stages," *IEEE Transactions on Circuits and Systems I: Regular Papers*, Vol. 71, No. 10, 4512–4523, 2024.

[7] Goyal, S., V. S. Kushwah, and V. V. Thakre, "Optimization of parallel coupled bandpass filter with CPW for UWB application," in *AIP Conference Proceedings*, Vol. 2816, No. 1, 200005, 2024.

[8] Dong, Q., Y. Wu, Z. Xu, W. Wang, and Q. Yang, "Miniaturized dual-band dielectric waveguide filter and dual-band filtering dielectric waveguide phase shifter," *AEU — International Journal of Electronics and Communications*, Vol. 158, 154462, 2023.

[9] Afridi, S., U. Ahmed, A. R. Gilal, J. Jaafar, I. A. Aziz, and M. Y. Sandhu, "High stop band rejection for ceramic loaded waveguide filters," *IEEE Access*, Vol. 8, 109 309–109 314, 2020.

[10] Hendry, D. R. and A. M. Abbosh, "Compact triple-mode band-stop ceramic cavity filters using parallel coupled resonators," *IEEE Microwave and Wireless Components Letters*, Vol. 29, No. 8, 526–528, 2019.

[11] Wu, X., Y. Cao, B. Yuan, Y. Qi, and G. Wang, "Novel compact bandpass filter using sextuple-mode ceramic cavity resonator," *Microwave and Optical Technology Letters*, Vol. 64, No. 11, 2000–2006, 2022.

[12] Wu, X., Y. Cao, B. Yuan, Y. Qi, and G. Wang, "Bandpass filters using single and cascaded novel triple-mode ceramic monoblocks," *IEEE Transactions on Components, Packaging and Manufacturing Technology*, Vol. 13, No. 7, 965–977, 2023.

[13] Richtmyer, R. D., "Dielectric resonators," *Journal of Applied Physics*, Vol. 10, No. 6, 391–398, 1939.

[14] Wang, X., K.-L. Wu, and W.-Y. Yin, "A novel surface-mounted monoblock dielectric filter," *IEEE Transactions on Components, Packaging and Manufacturing Technology*, Vol. 4, No. 11, 1822–1827, 2014.

[15] Chen, J.-X., Y. Zhan, W. Qin, Z.-H. Bao, and Q. Xue, "Novel narrow-band balanced bandpass filter using rectangular dielectric resonator," *IEEE Microwave and Wireless Components Letters*, Vol. 25, No. 5, 289–291, 2015.

[16] Xu, Z., Y. Wu, Q. Dong, and W. Wang, "Miniaturized dual-band filter using dual-mode dielectric waveguide resonator," *IEEE Microwave and Wireless Components Letters*, Vol. 32, No. 12, 1411–1414, 2022.

[17] Lee, T.-H., J.-W. Baik, and Y. Kim, "Compact cascaded quadruplet bandpass filter using artificial magnetic resonators," *Microwave and Optical Technology Letters*, Vol. 55, No. 4, 883–886, 2013.

[18] Rao, J., C. Sun, Z. Chen, B. Xue, G. Zhang, J. Hong, and K. Aliqab, "Analysis of the compact graded dumbbell coaxial resonator with its filter design applications," *IEEE Transactions on Microwave Theory and Techniques*, Vol. 72, No. 6, 3577–3587, 2024.

[19] Wu, J., M. Fu, D. Jia, Q. Feng, and Q. Xiang, "A U-band cascaded quadruplet quartz glass SIW filter based on double row vias coupling window," *AEU — International Journal of Electronics and Communications*, Vol. 181, 155358, 2024.

[20] Yan, J.-J., F.-C. Chen, K.-R. Xiang, and Z.-H. Tu, "Design of tunable coaxial bandpass filters with constant absolute bandwidth using one tuning element," *IEEE Transactions on Circuits and Systems II: Express Briefs*, Vol. 71, No. 4, 1959–1963, 2024.

[21] Yuan, B., "Dielectric filter, transceiver, and base station, 20200381795," United States Patent, https://ppubs.uspto.gov/basic/, 2020.

[22] Liang, F., S. Meng, and W. Lyu, "Design of microwave ceramic waveguide filter with high out-of-band suppression characteristics," *Journal on Communications*, Vol. 42, No. 4, 194–201, 2021.

[23] Meng, S., F. Liang, W. Lu, Z. Lin, Y. Yin, and R. Zhang, "Design of a microwave filter based on a novel negative coupling structure with conical through-hole," *China Communications*, Vol. 19, No. 2, 148–157, 2022.

[24] Du, Z., J. Pan, X. Ji, D. Yang, and X. Liu, "Ceramic dielectric-filled cavity filter," in *2020 IEEE 5th Information Technology and Mechatronics Engineering Conference (ITOEC)*, 888–891, Chongqing, China, 2020.

[25] Lu, D., B. Zhu, and M. Yu, "Electrically-tunable ceramic-waveguide filter," *Electromagnetic Science*, Vol. 2, No. 4, 1–10, 2024.

[26] Huang, Z. and Y. Cheng, "Cross-coupled dielectric waveguide filter," *International Journal of RF and Microwave Computer-Aided Engineering*, Vol. 31, No. 5, e22585, 2021.

[27] Yan, M. L., S. M. Zhang, Y. Cheng, *et al.*, "A novel triangular resonator filter based on cross-coupling," *Journal of Nanjing University of Posts and Telecommunications(Natural Science)*, Vol. 44, No. 5, 28–36, 2024.

[28] Byun, W.-J., B.-S. Kim, K. S. Kim, K.-C. Eun, M.-S. Song, R. Kulke, O. Kersten, G. Möllenbeck, and M. Rittweger, "40 GHz vertical transition with a dual-mode cavity for a low-temperature co-fired ceramic transceiver module," *ETRI Journal*, Vol. 32, No. 2, 195–203, 2010.

[29] Luhaib, S. W. O., M. S. Bakr, N. Somjit, and I. C. Hunter, "Design and characterisation of HE11 dual-mode dielectric-loaded filter for cellular base station applications," *International Journal of Electronics*, Vol. 106, No. 10, 1530–1542, 2019.